ACS Sustainable Chemistry & Engineering

pubs.acs.org/journal/ascecg

Research Article

Predicted Influence of Plasma Activation on Nonoxidative Coupling of Methane on Transition Metal Catalysts

Yannick Engelmann,* Prateek Mehta, Erik C. Neyts, William F. Schneider, and Annemie Bogaerts

Cite This: *ACS Sustainable Chem. Eng.* 2020, 8, 6043−6054

Read Online

ACCESS | Metrics & More | Article Recommendations | Supporting Information

ABSTRACT: The combination of catalysis and nonthermal plasma holds promise for enabling difficult chemical conversions. The possible synergy between both depends strongly on the nature of the reactive plasma species and the catalyst material. In this paper, we show how vibrationally excited species and plasma-generated radicals interact with transition metal catalysts and how changing the catalyst material can improve the conversion rates and product selectivity. We developed a microkinetic model to investigate the impact of vibrational excitations and plasma-generated radicals on the nonoxidative coupling of methane over transition metal surfaces. We predict a significant increase in ethylene formation for vibrationally excited methane. Plasma-generated radicals have a stronger impact on the turnover frequencies with high selectivity toward ethylene on noble catalysts and mixed selectivity on non-noble catalysts. In general, we show how the optimal catalyst material depends on the desired products as well as the plasma conditions.

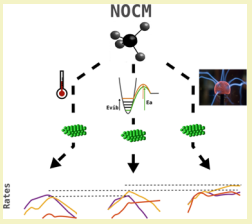

KEYWORDS: *plasma catalysis, microkinetic modeling, vibrational excitation, radicals, catalyst design*

Downloaded via PURDUE UNIV on March 17, 2021 at 17:42:28 (UTC).
See https://pubs.acs.org/sharingguidelines for options on how to legitimately share published articles.

INTRODUCTION

The price of methane is decreasing through technological improvement and recently discovered natural gas sources.[1,2] Methane is often produced at remote sites from where transportation is difficult. It is therefore desirable to reform methane to more readily transportable and valuable products,[2−5] such as olefins,[5,6] which are today primarily produced by steam cracking of higher hydrocarbons at elevated temperatures (∼900 °C).

The current routes of methane to olefins include[1,3] (i) reforming to synthesis gas (syngas) and subsequently syngas to methanol and methanol to olefin (MTO), (ii) reforming to syngas and syngas to olefin via Fisher−Tropsch synthesis (FTO), (iii) oxidative coupling of methane (OCM), and (iv) nonoxidative coupling of methane (NOCM). MTO and FTO are indirect and infrastructure-intense processes, and OCM consumes an oxidant and wastes some methane hydrogen as water. NOCM is a particularly appealing option as it potentially yields desired products in one step and avoids the need for an oxidant. Efficient NOCM to olefins is difficult to achieve thermally because equilibrium conversions become appreciable only above about 750 °C, and coking readily occurs at this and higher temperatures. Between 750 and 1200 °C, benzene is an important equilibrium product,[7] and dehydroaromatization over Mo-based catalysts is possible.[8,9]

NOCM is highly endothermic and energy-intensive when driven thermally, and thus, alternative approaches to activating and converting methane to useful products are in great need. Plasma activation provides one such potential avenue.[10] Methane is activated in both thermal and nonthermal plasmas through electron impact processes that could provide alternative routes to couple methane nonoxidatively.[3] At temperatures above 3000 °C, acetylene becomes the thermodynamically preferred product of methane decomposition.[11] The Hüels process plays on this thermodynamics by using a thermal plasma to generate the high temperatures necessary to drive equilibrium toward acetylene and hydrogen. Energy efficiencies and CH_4 conversions can reach 40 and 70%, respectively.[3] To avoid recombination of the products, the gases must be rapidly quenched before separation, and the process requires a regeneration step to remove carbon lay down from the electrodes.

Nonthermal plasmas (NTPs) operate at a much lower bulk temperature, and NTP-processing of methane has the potential benefit where thermodynamically unfavorable reactions become possible at lower temperatures due to the nonequilibrium nature of the system.[12−15] Scapinello *et al.*[3] compared the best energy efficiencies, CH_4 conversions, and product selectivities reported in the literature between different plasma sources for NOCM, including dielectric barrier discharges (DBDs), gliding arc plasmas, corona discharges, and microwave plasmas. DBDs are of particular interest because of their scalability from laboratory to industrial reactors and their operation at ambient pressures and temperatures.[16] NOCM in DBDs however suffers in terms of energy efficiency and CH_4 conversion, reaching values of around 3 and 10%, respectively.[3] Nozaki *et al.* predicted from a

Received: February 4, 2020
Revised: March 24, 2020
Published: March 30, 2020

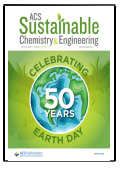

© 2020 American Chemical Society

https://dx.doi.org/10.1021/acssuschemeng.0c00906
ACS Sustainable Chem. Eng. 2020, 8, 6043−6054

numerical model[17] that, in a DBD, 36% of the input electrical energy is lost to vibrational excitations and subsequent vibrational−translational relaxation. Vibrational excitation of methane leading to gas-phase dissociation is slow due to the high energy barrier, while relaxation through gas-phase collisions happens significantly faster.[18] Several other works have studied NOCM in DBDs with kinetic models.[14,19,20] Each of these works studied the importance of both electron impact vibrational excitation as well as electron impact dissociation. Vibrational excitations of methane are found to be relatively unreactive in DBD plasma, and the most important loss terms for methane are direct electron impact dissociations. These works confirm the general trend in plasma-assisted NOCM and that, for a low specific energy input (SEI), the main products are ethane and propane, while at higher SEI, ethane is converted to acetylene. At low SEI, CH_3 radicals are generated through electron impact dissociations of methane, which recombine mostly to ethane. In higher SEI plasmas, ethane is mostly converted to acetylene because intermediate ethylene is readily dehydrogenated.[14] Yang[14] concluded that it is particularly difficult to produce ethylene. They suggested that, to improve ethylene selectivity, the electron energy should be carefully controlled to avoid ethane and acetylene formation, and specific neutral−neutral recombination reactions should be enhanced.

A potential approach to improving the performance of plasma-activated methane conversions is through coupling with a heterogeneous catalyst.[10,13,21,22] Plasma-assisted catalysis has been demonstrated for hydrocarbon reforming,[23] waste gas treatment,[24] CO_2 conversion,[10,22] NH_3 synthesis,[10,25] and methane conversions.[10,22] Mehta *et al.* reviewed the impact of plasma activation on catalytic methane dry reforming.[10] They highlighted the potential of plasma catalysis to allow chemical conversion to happen at lower temperatures where, thermally, no conversion is expected. At higher temperatures, plasma-activated species undergo thermal relaxation and the potential impact of the plasma on the conversion is cancelled. This trend was shown by Nozaki *et al.*[17] and Kim *et al.*[26,27] in their studies on methane steam and dry reforming, respectively. Nozaki *et al.* examined the influence of a DBD on the methane steam reforming performance over a Ni/SiO_2 catalyst.[17] They observed the methane conversion curve to shift about 200 °C to lower temperature in the presence of plasma as well as a positive correlation between plasma discharge power and methane conversion. Kim *et al.*[26,27] observed methane dry reforming yields over a Ni/Al_2O_3 catalyst to exceed that of bulk thermal equilibrium at temperatures of 400 to 600 K. They attributed the enhancements to methane vibrational excitations and their effect on the dissociation rate at the catalyst surface.

Only a limited number of studies has been reported for plasma-catalytic NOCM in gliding discharges and in DBDs.[28−31] To study the effect of catalyst material on the plasma, Jo *et al.*[28] examined the effect of electric conductivity of the catalyst on methane activation in a DBD. Their models show a lowering of the electric field upon introduction of an alumina-supported Pt catalyst compared to the electric field in the presence of bare alumina. The introduction of a conductive metal in the discharge zone results in higher CH_3 and lower CH densities. Consequently, they show higher selectivity to ethane and lower selectivity toward acetylene compared to the results on bare alumina. Schmidt-Szalowski[29] *et al.* and Mlotek *et al.*[30] studied the effects of transition metals in a combination of a gliding arc discharge and a mobile catalyst bed. They concluded that this setup is an effective way to perform NOCM to C_2 hydrocarbons. Schmidt-Szalowski attributed the changes in selectivity to electrical properties of the catalyst material and their effect on the discharge. Mlotek postulated that the change in selectivity in favor of ethane and ethylene was due to two possible reaction pathways: (i) plasma generation of CH_3 and CH_2 radicals that can couple readily to ethane and ethylene and (ii) hydrogenation of produced acetylene to ethane and ethylene in the presence of the catalyst. Spiess *et al.*[31] studied the impact of the electrode material in discharge plasmas on the methane conversion. Based on mass spectrometry and GC/MS data, they suggested plasma-catalytic reaction pathways for the different products. Their suggested pathways start from plasma-activated methane dissociating on the catalyst surface, initiating the radical reactions through creation of CH_3* and H*. Subsequent recombination and termination reactions also happen on the catalyst surface. The highest methane decomposition rates were observed on noble catalysts. Scapinello *et al.*[32] examined the impact of a copper rod along the centerline of a pulsed discharge reactor on the acetylene hydrogenation. They observed a significantly higher ethylene conversion around 200−400 °C compared to the conversion in the presence of a stainless steel rod or for homogeneous reactions.

All of these works show that it is important to pick the right catalyst material for the right plasma. However, a detailed insight in which reaction mechanisms are at play, how reaction mechanisms are impacted by the different metals, and how optimal catalyst materials can be chosen are still lacking. An impediment to answering these questions is the lack of models to relate catalyst composition to performance. In a recent study, Mehta *et al.*[33] reported a microkinetic model for ammonia synthesis that attempted to capture the potential influence of plasma excitation of N_2 vibrations on surface site-normalized reaction rates. Starting from a conventional, thermal-only microkinetic model for the rate of ammonia synthesis versus a catalyst characteristic, in this case, the binding energy of atomic nitrogen (N*), they augmented this thermal model with estimates for the extent of nonthermal N_2 vibrational excitation based on laboratory observation of the apparent N_2 vibrational temperature and an estimate of the consequences of vibrational excitation on the N_2 dissociative sticking coefficient. Ensemble averaging over vibrational states yielded a predicted plasma-enhanced ammonia synthesis rate. Model results were consistent with the observed ability of the plasma−catalyst combination to produce ammonia at conditions that are thermally inaccessible, and they predicted that the optimal catalytic material (the "peak" in the volcano) is shifted to lesser absolute N* binding energy. Experimental observations were consistent with this predicted shift. A follow-up work[34] showed the potential to surpass the thermodynamic conversion limit when coupling the plasma with the right catalyst. The presence of a nonthermally activated reaction channel can kinetically trap the produced ammonia at higher than thermal equilibrium limits. For catalysts with lower N* binding energy, the beyond equilibrium effect was observed at lower levels of N_2 excitation.

Methane is similarly known to become vibrationally activated in plasmas. Further, vibrational excitations are well known to influence the rate of methane dissociation on transition metal catalysts.[35] However, to the best of our knowledge, no research has been done on how these

https://dx.doi.org/10.1021/acssuschemeng.0c00906
ACS Sustainable Chem. Eng. 2020, 8, 6043−6054

vibrational excitations impact NOCM in the context of plasma-activated catalysis. Additionally, while the above-mentioned works on plasma-catalytic NOCM highlight the importance of radical densities in the plasma phase, none of these works provide direct mechanistic and kinetic insight into the surface catalytic chemistry. For these reasons, we develop, in this work, microkinetic models for NOCM on transition metal surfaces, incorporating (i) the influence of vibrational excitations and (ii) the influence of plasma-generated radicals on methane dissociation rates. We use DFT results available in the CatApp database[36] to parameterize surface reaction rates. We take advantage of observed correlations between reaction and activation energies to relate results to a single descriptor of surface reactivity.[37,38] We incorporate the influence of methane vibrational excitations and plasma-generated radicals on the reaction mechanisms and rates. We solve the model at 500 K and 1 bar to simulate the reaction conditions in a DBD packed with a transition metal catalyst. It is our aim to compare the impact of vibrational excitations and of plasma-generated radicals in plasma-catalytic NOCM with thermal catalytic NOCM. The plasma and catalyst are otherwise decoupled to focus on the chemistry of the aforementioned plasma species. This way, we provide essential information for understanding the specific concepts in plasma-catalytic NOCM and plasma catalysis in general. Our results encompass a comparison of methane conversion rates, product selectivity, catalyst coverage, and reaction mechanisms.

MICROKINETIC MODEL CONSTRUCTION AND SOLUTION

We developed a mean-field microkinetic model[33,39] to simulate thermal NOCM as well as NOCM with vibrationally excited methane and NOCM with plasma-generated radicals. We constructed a set of rate equations to compute the reaction kinetics on transition metal catalysts in contact with methane. These rate equations are differential equations for the time derivative of the surface coverages

$$\frac{\partial \theta_i}{\partial t} = \sum_j c_{ij} \cdot r_j \tag{1}$$

where θ_i is the surface coverage of adsorbate i (defined as the total number of adsorbed species divided by the total number of adsorption sites), c_{ij} is the stoichiometric coefficient for the adsorbate in surface reaction j, and r_j is the rate (in coverage·s^{-1}) corresponding to this reaction, which is defined as

$$r_j = k_{j,\mathrm{f}} \prod_s a_s^{c_{sj,\mathrm{f}}} - k_{j,\mathrm{r}} \prod_s a_s^{c_{sj,\mathrm{r}}} \tag{2}$$

with $k_{j,\mathrm{f}}$ and $k_{j,\mathrm{r}}$ being the forward and reverse reaction rate coefficients, respectively, a_s is the activity of species s (equal to the coverage in case of adsorbates and to the pressure in bar in case of gas-phase species), and $c_{sj,\mathrm{f}}$ and $c_{sj,\mathrm{r}}$ are the stoichiometric coefficients of the reactants of the forward and the reverse reactions, respectively. The reaction rate coefficients $k_{j,\mathrm{f}}$ and $k_{j,\mathrm{r}}$ are calculated with harmonic transition state theory using the Eyring–Polanyi equation

$$k_{\mathrm{TST}} = \frac{k_\mathrm{B} T}{h} e^{\Delta S^\ddagger / R} e^{-\Delta H^\ddagger / RT} \tag{3}$$

Here, k_B is the Boltzmann constant, h is Planck's constant, and $\Delta S^\ddagger$ and $\Delta H^\ddagger$ are the entropy and enthalpy barriers to the transition state, respectively.

To incorporate the influence of plasma-induced vibrational excitations on CH_4 dissociation rates, we assign a vibrational temperature ranging from 500 to 3000 K, distinct from the bulk temperature, and assume the vibrational states follow a Boltzmann distribution.[40] Activation barriers, $\Delta H^\ddagger$, are decreased proportional to the excitation energy (E_ν) formulated by the following equations

$$k_{\mathrm{TST},\nu} = \frac{k_\mathrm{B} T}{h} e^{\Delta S^\ddagger / R} e^{-(\Delta H^\ddagger - \alpha E_\nu)/RT}$$
$$k_{\mathrm{TST}} = p(\nu) k_{\mathrm{TST},\nu}$$
$$p(\nu) = \frac{e^{-E_\nu / k_\mathrm{B} T}}{\sum e^{-E_\nu / k_\mathrm{B} T}} \tag{4}$$

where α is a function of the forward activation barrier, E_a^f, and the backward activation barrier, E_a^b, as defined by the Fridman–Macheret equation[41]

$$\alpha = \frac{E_\mathrm{a}^\mathrm{f}}{E_\mathrm{a}^\mathrm{f} + E_\mathrm{a}^\mathrm{b}} \tag{5}$$

We chose to neglect the impact of the $\nu_{2,4}$ bending modes of methane because no alpha parameter is known for the excitation of these modes. On the one hand, the efficacy of these modes is generally lower than that of the stretch modes,[35] but the spacing between the energy levels is also much lower, resulting in higher populations of the higher energy levels. Juurlink *et al.*[35] reported high energy efficacies toward methane dissociation for the vibrational excitation of the ν_1 symmetric stretch and the ν_3 asymmetric stretches. They noted that the excitation of the $\nu_{2,4}$ bending modes can aid in a better access of the transition state but that their efficacies are typically lower. In any case, the aim of our work is to study the impact of vibrational excitations in a qualitative way. Depending on the exact vibrational distribution function and on how the efficacies change over the different levels of excitation and catalyst materials, the maximum turnover rates might be shifted to higher/lower temperatures or to higher/lower binding energies, but the general trends remain unchanged. In the Supporting Information (Figures S1 and S2), we compare the effect of the bending modes, assuming alpha parameters equal to 0.1 and 0.5.

We solved the ordinary differential rate equations on the most noble catalyst (E_b = 1 eV) until the surface coverage reached a steady state ($\partial\theta_i/\partial t$ = 0 for all species i). In subsequent steps, E_b is decreased in increments of −0.01 eV until E_b = −1 eV. During each iteration, new reaction barriers and the corresponding reaction rate coefficients are calculated, and the steady state of the previous step is used as a guess to solve for an algebraic solution. This solution is inserted back into the rate equations to obtain steady-state turnover frequencies (TOFs).

RESULTS AND DISCUSSION

Reactions and Reaction Parameters. We seek to build the simplest possible microkinetic model for C–C coupling starting from methane at a transition metal surface. We choose transition metals both because plasma-promoted NOCM is observed over transition metal catalysts[30] and because parameters for microkinetic models are available from literature tabulations. We assume CH_4 as a reactant, C_2 hydrocarbon species as products, and adsorption/desorption,

https://dx.doi.org/10.1021/acssuschemeng.0c00906
ACS Sustainable Chem. Eng. 2020, 8, 6043−6054

Table 1. Surface Reaction Steps and Associated Microkinetic Parameters on the (211) Steps

reaction step	γ_f	ξ_f	MAE	γ_a	ξ_a	MAE
adsorption/desorption						
$H_{(g)} + * \rightleftharpoons H*$	0.73	−2.49	0.10	0.00	0.00	0.00
$H_{2(g)} + 2* \rightleftharpoons 2H*$	1.46	−0.45	0.20	0.86	0.49	0.15
$C_{(g)} + * \rightleftharpoons C*$	3.05	−5.03	0.27	0.00	0.00	0.00
$CH_{(g)} + * \rightleftharpoons CH*$	2.59	−4.66	0.18	0.00	0.00	0.00
$CH_{2(g)} + * \rightleftharpoons CH_2*$	1.82	−3.15	0.19	0.00	0.00	0.00
$CH_{3(g)} + * \rightleftharpoons CH_3*$	1.00	−1.52	0.00	0.00	0.00	0.00
$CH_{4(g)} + 2* \rightleftharpoons CH_3* + H*$	1.73	0.55	0.10	1.41	1.29	0.13
$C_2H_{(g)} + * \rightleftharpoons C_2H*$	2.98	−2.75	0.24	0.00	0.00	0.00
$C_2H_{2(g)} + * \rightleftharpoons C_2H_2*$	2.52	−0.10	0.20	1.08	0.46	0.25
$C_2H_{3(g)} + * \rightleftharpoons C_2H_3*$	0.93	−1.46	0.22	0.00	0.00	0.00
$C_2H_{4(g)} + * \rightleftharpoons C_2H_4*$	0.80	0.04	0.17	0.34	0.17	0.06
$C_2H_{5(g)} + * \rightleftharpoons C_2H_5*$	1.30	−1.35	0.12	0.00	0.00	0.00
(de)hydrogenation						
$C* + H* \rightleftharpoons CH* + *$	−1.19	−0.67	0.20	−0.35	0.99	0.16
$CH* + H* \rightleftharpoons CH_2* + *$	−1.50	−0.39	0.20	−0.40	0.97	0.29
$CH_2* + H* \rightleftharpoons CH_3* + *$	−1.55	−0.69	0.27	−0.15	0.47	0.08
$C_2H* + H* \rightleftharpoons C_2H_2* + *$	−1.19	−0.67	0.20	−0.35	0.99	0.16
$C_2H_2* + H* \rightleftharpoons C_2H_3* + *$	−2.32	−0.39	0.29	−0.40	0.97	0.29
$C_2H_3* + H* \rightleftharpoons C_2H_4* + *$	−0.86	−0.84	0.11	−0.15	0.47	0.08
$C_2H_4* + H* \rightleftharpoons C_2H_5* + *$	−0.24	−0.46	0.12	−0.02	0.74	0.09
$C_2H_5* + H* \rightleftharpoons C_2H_{6(g)} + 2*$	−2.03	−0.55	0.05	−0.29	0.67	0.02
carbon coupling						
$2CH* \rightleftharpoons C_2H_2* + *$	−2.66	−0.78	0.32	−0.98	1.28	0.25
$2CH_2* \rightleftharpoons C_2H_4* + *$	−2.83	−1.24	0.52	−0.94	0.65	0.31
$2CH_3* \rightleftharpoons C_2H_{6(g)} + 2*$	−2.00	−0.87	0.00	−0.44	2.08	0.18

(de)hydrogenation, and carbon coupling reactions as summarized in Table 1. Jo *et al.*[28] reported that C_2 hydrocarbons were produced with ∼70% selectivity, depending on the discharge power, in DBDs packed with alumina-supported Pt. The given chemistry set is a subset of a large amount of species and reactions occurring in plasma-catalytic NOCM, but it allows studying the specific role of plasma-generated species including vibrationally excited CH_4 and plasma-generated radicals. We referred to the CatApp database[36] of the DFT-computed reaction and activation energies to parameterize microkinetic models. We built scaling relations for the reactions in Table 1 based on the reaction and activation energies computed using the RPBE functional on the (211) steps of Ru, Rh, Pt, Cu, Au, and Ag. In the Supporting Information, Figures S3 to S8, we plotted the reaction and activation energies against the binding energy of CH_3 (E_b) for all the reactions in Table 1 for the (211) steps and the (111) terraces, respectively. Consistent with the literature, we find approximately linear correlations between all steps. The linear fit parameters, γ and ξ, for the forward reaction energy, E_f, and the activation barrier, E_a, are listed in Table 1 for each reaction along with the mean absolute error (MAE) following the equations

$$E_f = \gamma_f \cdot E_b + \xi_f \tag{6}$$

$$E_a = \gamma_a \cdot E_b + \xi_a \tag{7}$$

$$\mathrm{MAE} = \frac{\sum_i^n |x_i - y_i|}{n} \tag{8}$$

With x_i being the literature value of the energy on transition metal i and y_i being the energy obtained when inserting E_b of metal i in the linear fit. In the table, the asterisk (*) symbolizes an adsorption site on the catalyst, and $A*$ is an adsorbate attached to one of these sites. The MAE is for all reactions similar to MAEs reported in the previous work on scaling relations.[38] Only the coupling reaction of 2 CH_2* to C_2H_4* has a higher MAE. Because binding energies on a given metal are taken to be linearly correlated, the underlying scaling relations are insensitive to the choice of binding energy. Meanwhile, for the thermal case, CH* is the more important species, but it is not for the other cases. CH_3* was chosen as it is the product of the first dehydrogenation of methane.

Throughout the paper, plasma−catalyst interactions other than the chemical behavior of specific plasma species on the catalyst surface are beyond the scope of this work. In reality, introducing different transition metals in the plasma zone will impact the plasma characteristics, while at the same time, the plasma will change catalyst surface characteristics, as explained in the Introduction and the references therein.

The entropy of the gas-phase species is calculated with the formula

$$S(T) = S^\circ_{298K} - S_{trans}(298\ \mathrm{K}) + S_{trans}(T) \tag{9}$$

where the standard gas-phase entropy, S°_{298K}, can be found in the database of the National Institute of Standards and Technology (https://webbook.nist.gov/chemistry/), and $S_{trans}(T)$ is the translational part of the entropy at temperature T[42]

$$S_{trans}(T) = R \ln\left(\frac{k_B T}{p}\frac{(2\pi m k_B T)^{3/2}}{h^3} e^{5/2}\right) \tag{10}$$

The rotational, vibrational, and electronic parts are assumed to stay constant in the temperature range. We note that the entropies of the stable molecules (i.e., H_2, CH_4, C_2H_6, C_2H_4, and C_2H_2) are known, but not of all the radicals in the model

https://dx.doi.org/10.1021/acssuschemeng.0c00906
ACS Sustainable Chem. Eng. 2020, 8, 6043−6054

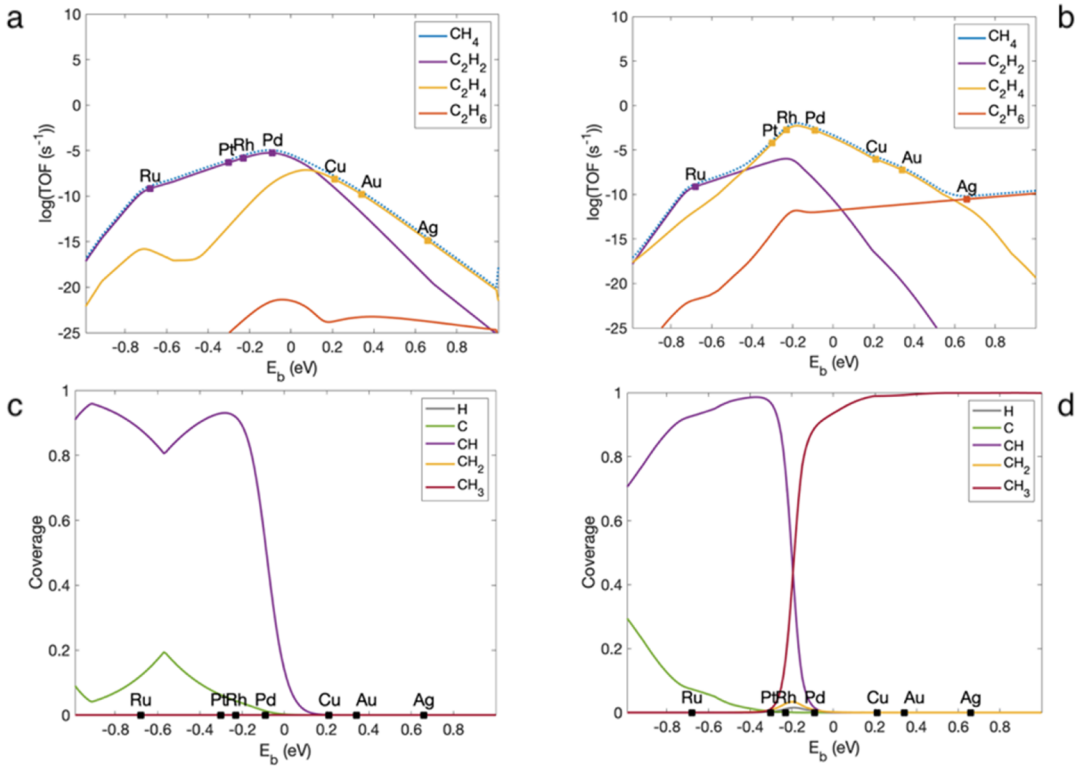

Figure 1. Steady-state (a, b) TOFs and (c, d) coverages vs descriptor (E_b) of NOCM in (a, c) thermal catalysis and with vibrationally excited CH_4 following a (b, d) Boltzmann distribution at T_{vib} = 1500 K.

(at a given temperature). For the sake of internal consistency, all the entropies were calculated with the formula above. To check the validity of this approach, we compared the calculated entropies for these stable molecules with the experimental values from literature, and we found an MAE at 500 K of 14 J mol^{-1} K^{-1} (Table S2 in the Supporting Information), which corresponds to a maximum error on the free energy barriers of 0.07 eV. We assumed that the entropy of the transition state is the entropy of a 2D gas for the case of radical adsorption/desorption ($X_{(g)}$ + * ⇌ X*) and equal to the surface entropy in the case of all other reactions.[42] Entropies of the surface species are varied linearly from a 0D gas for the strongly binding catalysts up till the entropy of a 2D gas for the weakly binding catalysts. Indeed, when the species are more strongly bound, they have more difficulty overcoming diffusion barriers, while less strongly bound species can move around more freely on the surface, behaving like a 2D gas.[42] The entropy of a 2D gas is equal to two-thirds of the entropy of a 3D gas, $S_{trans}(T)$. The linear scaling correlates the surface entropy to our independent descriptor, the binding energy of CH_3, so that all rate coefficients can still be calculated as function of a single parameter.

We solved for steady-state reaction rates at 1 bar CH_4, 500 K, and zero conversion, as described in the *Microkinetic Model Construction and Solution*. The reported rates can be interpreted as the rates at the front of a PFR or in a CSTR where the residence time is vanishingly small or the volume is much greater than the amount of the catalyst. Because we assume zero conversion, the system is necessarily away from equilibrium and the rates correspond to the initial forward rates toward said equilibrium. We find that rates on the stepped surfaces are several orders of magnitude greater than on the terraces, but otherwise, follow similar trends. We report the stepped surface results here in the main article and include the results on the metal terraces in the Supporting Information (Figures S9 to S11).

Thermal Nonoxidative Coupling. The left side plots in Figure 1 show the computed steady-state TOFs (top) and coverages (bottom) for thermal catalytic NOCM at 500 K with a gas-phase composition equal to 1 bar of methane at 0% conversion. The TOF is defined as

$$\text{TOF}\ (s^{-1}) = \frac{\text{number of produced molecules}}{\text{number of sites}\cdot\text{second}} \qquad (11)$$

The results are shown as a function of the binding energy of CH_3 (ranging from strongly binding catalysts on the left to weakly binding catalysts on the right). Species that are produced are displayed with a full line, while consumed species (in this case, methane) are displayed in a dotted line.

We observe a maximum methane conversion rate at −0.1 eV, close to the Pd catalyst. The TOF of NOCM follows a volcano-like behavior. On the right side of the plot, where the catalysts bind weaker, the dissociation of CH_4 to CH_3 and H is the rate-limiting step because the TOF is equal to the methane dissociation rate. The linear scaling relations that were constructed for the reaction barriers result in an exponential increase of the reaction rate coefficients. On a logarithmic scale, this results in a linear increase as the catalysts bind species more strongly. On the left flank of the volcano, methane conversion is rate limited by product formation. In the range of −0.1 to −0.7 eV, the TOF is equal to the reaction rate coefficient of acetylene desorption (C_2H_2* → $C_2H_{2(g)}$), being the rate-limiting step in this region. At −0.7 eV, the volcano shows a discontinuity in the slope. For more strongly binding catalysts, the rate-limiting step is no longer the

https://dx.doi.org/10.1021/acssuschemeng.0c00906
ACS Sustainable Chem. Eng. 2020, 8, 6043−6054

desorption of C_2H_2* but the formation of C_2H_2* through coupling of 2 CH*.

C_2 species can be formed along (i) the carbon coupling pathway, where CH_y (de)hydrogenation precedes C−C coupling and (ii) the (de)hydrogenation pathway, where coupling precedes dehydrogenation of C_2H_y species to the final product. For ethylene and ethane, the combination of these two pathways leads to "dual volcanos". In the case of ethylene, the summit of the highest volcano can be found around 0 eV. This volcano corresponds to the coupling of CH_2* radicals. The second summit occurs at −0.7 eV where the dominant pathway is C_2H_2* hydrogenation to C_2H_4*. Similarly, the dual volcano behavior can also be observed for ethane. On the more weakly binding catalysts (from 0 to 1 eV), a volcano trend occurs from the coupling of CH_3* radicals, while around −0.1 eV, a higher volcano occurs for the hydrogenation of C_2H_4* to C_2H_6. The individual rate of each elementary reaction in the model is reported in the Supporting Information (Figure S12). From these plots, it can be determined which are the dominant reactions for gain and loss terms of the species. Volcano behavior of methane conversion was reported before in methane steam reforming.[43] To the best of our knowledge, these are the first reports of volcano plots for NOCM.

On the bottom left plot, we can see that, for all catalysts with a binding energy greater than Pd, the active sites remain empty as all the CH_3* radicals get dehydrogenated to CH_2*, which couple to form C_2H_4 before a new CH_4 molecule can dissociate. On more strongly binding catalysts, the most stable adsorbates are CH* (and to some extent, C*). The same discontinuity as mentioned above, arising from a change in the rate-limiting step, can be observed in the steady-state coverage of CH* as well. Since it becomes more difficult for CH* to couple to C_2H_2*, there is a temporary increase of the steady-state coverage in the interval from −0.5 to −0.9 eV.

The net steady-state rates along the different reaction pathways in NOCM are shown in Figure 2 for rhodium (E_b = −0.24 eV) and silver (E_b = 0.65 eV). The intermediate species C_2H_5*, C_2H_3*, and C_2H* are left out for the sake of clarity. The width of the flow lines corresponds to the relative weights, but as the latter can vary up to 10 orders of magnitude, the widths are not drawn to scale. However, they still show a good overview of the dominant pathways. For the exact values of the net rates of each reaction, we refer to Figures S12 to S14 in the Supporting Information. The diagrams confirm that, on the more strongly binding catalyst (Rh), the (blue) dehydrogenation flow lines are more important up to CH* and push the conversion toward acetylene, while on the more noble catalyst (Ag), the largest flow ends in ethylene in agreement with the volcano plot in Figure 1 (top left plot). Furthermore, CH_3 coupling is more important than the C_2H_4 hydrogenation pathway for the formation of C_2H_6 on Ag (red flow lines), while the opposite holds for Rh. The shift from one dominant pathway to the other translates in the dual volcano behavior explained above. A small part of C_2H_4 is dehydrogenated to C_2H_2 on Ag (purple flow line between both), while on Rh, the direction of the pathway is inverted and C_2H_4 is formed from C_2H_2 hydrogenation (yellow flow line between both). This result, showing that C_2H_4 (de)hydrogenation acts as an important branching mechanism in the catalytic conversion, was also suggested by Indarto *et al.*[19] for plasma-based conversion based on a microkinetic model for NOCM in a DBD (without a catalyst).

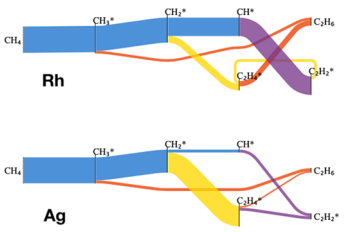

Figure 2. Relative weights of reaction pathways in thermal catalytic NOCM using a flow diagram representation.[44] Blue flow lines represent dehydrogenation, while red, yellow, and purple flow lines represent the formation of ethane, ethylene, and acetylene, respectively.

Effect of Methane Vibrational Excitation. We next incorporate the influence of CH_4 vibrational excitation on rates and selectivities. Vibrational excitations are expected not only to be prominent in microwave and gliding arc plasmas[12,15] but also they can be important in dielectric barrier discharges (DBDs),[17] depending on the power distribution over the microdischarge filaments. In addition, vibrational excitation can also be realized, e.g., by lasers,[35] making it of broader fundamental interest.

The right-hand side of Figure 1 reports turnover frequencies and steady-state coverages obtained from methane vibrational excitation. The vibrationally excited methane follows here a Boltzmann distribution at a vibrational temperature of 1500 K. This temperature was found to give the highest TOF, as shown in Figure 4 and explained below.

In the bottom right graph, a notable difference can be seen in the steady-state coverage of CH_3* on the more noble catalysts. The reactive methane molecules dissociate much faster than in the thermal case due to the vibrational excitation. Therefore, these catalysts, which are not capable of dehydrogenating CH_3* to CH_2*, are completely covered with CH_3* radicals. Around Pd and Rh, the steady-state coverage shifts in favor of CH*.

On the turnover frequency plots, we observe important changes in the selectivity of the C_2 hydrocarbons. The major product formed from vibrationally activated NOCM is ethylene for most of the catalysts (Pt, Rh, Pd, Cu, and Au) with the exception of Ag, which mainly produces ethane, and Ru, for which acetylene is predicted to be the major product. From this perspective, combining vibrational excitations of methane with the appropriate catalyst is a promising way to favor ethylene production, which is of particular interest for the chemical industry. Increased methane conversion rates are found for those catalysts where CH_4 dissociation was rate-limiting (Pd, Cu, Au, and Ag) and on Pt and Rh where the rate-limiting step has shifted from CH* to CH_2* coupling. On Ag, the rate-limiting step is now the coupling of CH_3* to ethane. We can see that the maximum ethane formation has increased and shifted to the more noble catalysts, while the volcano for ethylene formation finds its maximum between Rh and Pd, similar to the thermal maximum. We observe a rate of ethylene formation that is a factor 10^5 higher around platinum, rhodium, and palladium. This increase is however not as high as for ethane (factor 10^{12}) since the conversion still depends on the ability of the catalyst to dehydrogenate CH_3*. The maximum TOF of acetylene does not change much, but the entire volcano lies slightly lower because of the lowered coverage of CH* around Pd and Rh.

https://dx.doi.org/10.1021/acssuschemeng.0c00906
ACS Sustainable Chem. Eng. 2020, 8, 6043−6054

As mentioned before, the ethane formation rate is the sum of two rates corresponding to two different pathways for product formation: one for the carbon coupling reaction (2 CH_3* to C_2H_6) and one for the two-step hydrogenation reaction (C_2H_4* and 2H* to C_2H_6). The top of the carbon coupling volcano has shifted from 0.4 eV (close to Au) in thermal NOCM to beyond 1 eV. Thus, catalysts that were inactive in thermal NOCM are now capable of reforming methane because they are no longer limited by low methane dissociation rates. The local maximum from the C_2H_4* hydrogenation pathway is still visible around −0.2 eV. On all catalysts, the ethylene conversion is now dominated by the CH_2* coupling mechanism, and the local maximum at −0.7 eV from the hydrogenation pathway, observed in thermal NOCM, is now lower than the local coupling rate of CH_2*. The individual rate of each elementary reaction in the model is reported in the Supporting Information (Figure S13).

The flow diagrams for NOCM with vibrationally excited methane are shown in Figure 3 for the Rh and Ag catalysts.

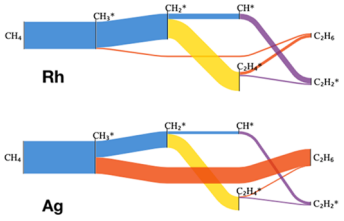

Figure 3. Relative weights of reaction pathways in NOCM with vibrationally excited methane using a flow diagram representation.[44] Blue flow lines represent dehydrogenation, while red, yellow, and purple flow lines represent the formation of ethane, ethylene, and acetylene, respectively.

The main difference between the thermal case and the case of vibrationally excited methane is the increased ethane TOF on noble catalysts (like Ag) due to the high amounts of CH_3* (see the right side plots of Figure 1). On Ag, the ethane TOF is higher than the TOF of ethylene, which is the second main product. The top of the volcano plot can be found on Rh where the main reaction path is CH_4 dissociation to CH_3*, CH_3* dehydrogenation to CH_2*, and subsequent CH_2* coupling toward ethylene. The primary pathway for ethane formation is C_2H_4* hydrogenation, instead of CH_3* coupling, which translates in the dual volcano behavior described above.

Figure 4 shows the maximum TOFs of methane, ethane, ethylene, and acetylene as a function of the vibrational temperature and the CH_3 binding energy. On the methane map, the summit is located at 1500 K around the −0.1 eV catalyst (close to Rh and Pd) where the main product is ethylene. The volcano plots corresponding to this vibrational temperature are the ones shown in the right-hand plots of Figure 1. At higher vibrational temperatures, the higher dissociation rate of methane results in a higher coverage of the catalyst. The lack of free sites obstructs the further dehydrogenation of CH_3 radicals to CH_2, thereby inhibiting the formation of ethylene and acetylene. These trends can also be verified on the ethylene map and even stronger on the acetylene map, which hardly benefits from vibrational excitations of the reactant. Figure S15 of the Supporting Information shows the same plots for the metal (111) terraces.

Effect of Reactive Plasma Species. The vibrational temperature used above was below the threshold for significant gas-phase CH_4 dissociations.[45] However, in practice, radicals are formed in DBD plasma by other processes, such as electron impact dissociation. We therefore now consider the potential effect of ground-state intermediate plasma species (radicals) and methane conversion products by modifying the gas-phase composition to the calculated pressures, characteristic for an atmospheric DBD at a temperature of 500 K[20]. While the exact partial pressures depend on the type of plasma, the qualitative trends and concepts described below are more generally valid.

The partial pressures of the relevant plasma species considered in the model are shown in Table 2. We neglect vibrational excitations here to focus on the contrast between plasma-accelerated surface reactions and plasma-generated species. It is indeed an advantage of computer modeling to be able to distinguish between separate effects, which is much more difficult in experiments. The reactions and the treatment of these extra species are outlined in the first paragraph of the section Results and Discussion. The only difference with the previous sections is that other species than methane can now also adsorb on the surface. Subsequent elementary reactions are identical as before.

In Figure 5, we show the steady-state turnover frequencies and coverages at 500 K for a gas mixture of methane, ethane, ethylene, and acetylene as well as the corresponding radicals based on their partial pressures (number densities) calculated for a DBD plasma (cf. Table 2 above).

On the right-hand side, we can see that the steady-state coverages are completely changed. In the thermal case, CH* (and to some extent C*) covered the surface of catalyst materials that bind more strongly than Pd. In the present case, where much more reactive carbon species are present in the gas phase, the more weakly binding catalysts (i.e., Cu, Au, and Ag) are covered with C_2H_3*, while the intermediate catalysts (including Pt, Rh, and Pd) are covered with C_2H_5*, C_2H_3*, and CH*, and the strongest catalysts (Ru and stronger) are covered with CH* and C_2H_2*. Indeed, the high amount of H and H_2 in the gas phase (see Table 2) hydrogenates the surface species, giving rise to more volatile species at the surface as compared to C* and CH* in the case of pure methane (either thermal or with vibrational excitation; cf. Figure 1). C_2H_5* and C_2H_3* are the dominant adsorbates because of their high densities in the plasma phase. Around Ru, a spike of adsorbed C_2H_2* can be observed. As mentioned above for thermal NOCM, in this regime, acetylene desorption becomes more difficult, resulting in a higher coverage of the species. On even stronger catalysts, acetylene breaks up in 2 CH* radicals. The interaction of plasma-generated radicals with the catalyst causes more saturated (and volatile) species to cover the surface, thus limiting the carbon laydown. The model captures the initial formation of carbonaceous species as chemisorbed C* and CH*, species expected to be precursors to coke. The model does not capture the further nucleation and growth of coke, which leads both to catalyst deactivation and non-productive methane consumption. Robust models for the rate of coke formation versus metal are not available. While carbon deposition is a major practical limitation in thermal NOCM, a potential advantage of plasma-enhanced methane conversion is the ability to operate at lower temperatures at which coke production rates are lower.

From the plot, it is clear that TOFs of the C_2 hydrocarbons have strongly increased compared to thermal NOCM with TOFs in the range of 10^{-2} around Pt and 10^3 around Ag. Hence, while for all catalysts investigated, the catalyst is almost

https://dx.doi.org/10.1021/acssuschemeng.0c00906
ACS Sustainable Chem. Eng. 2020, 8, 6043−6054

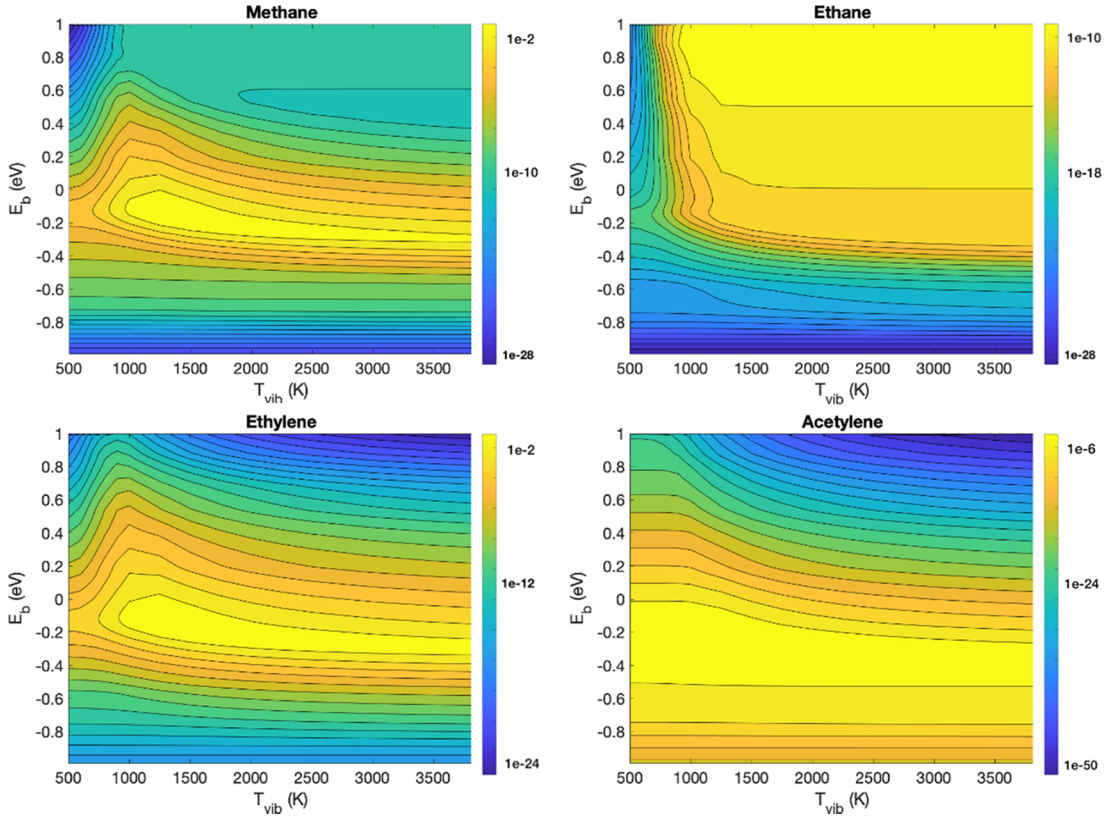

Figure 4. log(TOF) as a function of T_{vib} and E_b (colors are assigned relative to the maximum TOF).

Table 2. Calculated Partial Pressures (bar) in a Methane DBD Plasma at 500 K, Adopted from De Bie *et al.*[20]

H			H_2	
1.06×10^{-8}			4.35×10^{-1}	
C	CH	CH_2	CH_3	CH_4
4.72×10^{-13}	1.34×10^{-12}	4.56×10^{-8}	2.01×10^{-8}	4.72×10^{-1}
C_2H	C_2H_2	C_2H_3	C_2H_4	C_2H_5	C_2H_6
1.04×10^{-11}	3.75×10^{-2}	2.02×10^{-5}	1.05×10^{-2}	3.03×10^{-5}	4.42×10^{-2}

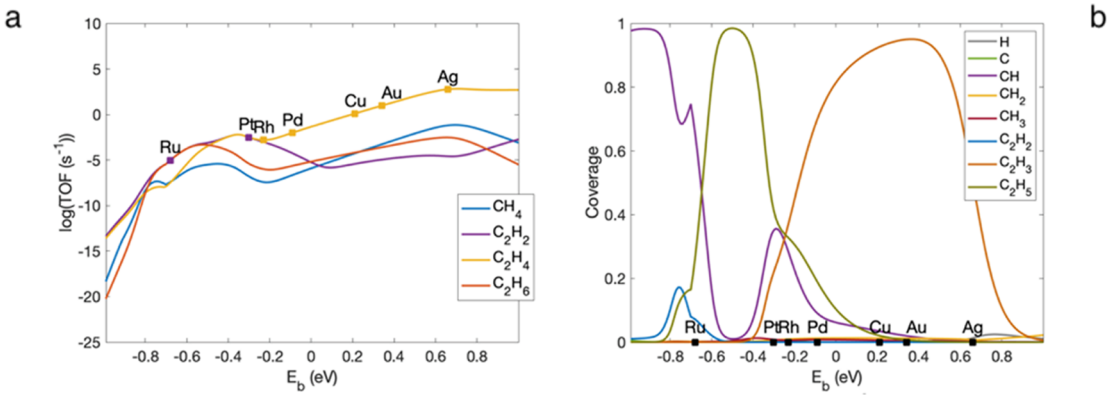

Figure 5. Steady-state (a) TOFs and (b) coverages vs descriptor (E_b) in NOCM with reactive plasma species, characteristic for a DBD plasma at 500 K.

completely covered with carbon species, and this only seems to inhibit the conversion process significantly on catalysts stronger than Rh. Most of the surface species on the more noble catalysts are C_2H_5* and C_2H_3*, which hydrogenate relatively easily toward ethane and ethylene. Because CH, CH_2, C_2H, and C_2H_3 are now present in the initial gas mixture (produced in the plasma), strongly binding catalysts are now no longer a requirement for their formation. On the weakly binding catalysts, C_2H* and C_2H_3* need H* atoms on the catalyst surface for contributing to the total C_2H_2 and C_2H_4 production, but the high densities of H atoms in the plasma phase can provide for these. C_2H_3 and CH_2 have considerably

https://dx.doi.org/10.1021/acssuschemeng.0c00906
ACS Sustainable Chem. Eng. 2020, 8, 6043−6054

higher densities than C_2H and CH (cf. Table 2 above) and, therefore, ethylene is the dominant product over acetylene for the more noble catalysts (Pd, Cu, Au, and Ag). Furthermore, as the CH_2 density is similar to the CH_3 density (and likewise for C_2H_3 and C_2H_5), ethylene is also preferred over ethane due to its lower formation barrier. Considering the added value of olefins, our results suggest that the more noble catalysts, maximizing ethylene TOF and selectivity, are most appropriate for NOCM in plasma with high densities of reactive radicals.

On the left side of the plot, reaction mechanisms are different, and ethane, ethylene, and acetylene have similar/identical TOFs. Indeed, around Pt and Rh, ethylene is formed through the hydrogenation of C_2H_3*. The H atoms necessary for this reaction are provided by the dehydrogenation of another C_2H_3* radical, resulting in a net reaction of $2C_2H_3$* radicals into C_2H_4 and C_2H_2 and an overlap of the TOFs of ethylene and acetylene in this region. Similarly, around Ru, C_2H_3* provides the hydrogen for the hydrogenation of C_2H_5*, yielding a net reaction of C_2H_3* + C_2H_5* into C_2H_2 and C_2H_6. The individual rate of each elementary reaction in the model is reported in the Supporting Information (Figure S14).

In general, the TOFs are dominated by the reactions of the plasma-produced radicals. The catalytic dissociation of methane is negligible, and the reverse reaction, which converts plasma-generated CH_3 back to methane, is faster on each catalyst material.

In Figure 6, we show the reaction pathways and their corresponding weights on Rh and Ag. The biggest difference

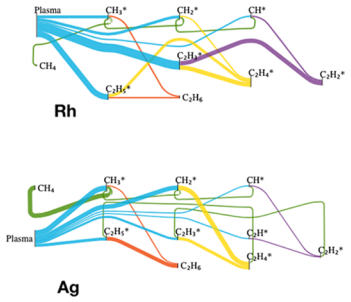

Figure 6. Relative weights of reaction pathways in plasma-catalytic NOCM using a flow diagram representation.[44] Green flow lines represent hydrogenation, red, yellow, and purple flow lines represent the formation of ethane, ethylene and acetylene, respectively, while light blue flow lines represent adsorption from species provided by the plasma. All reactions flow from left to right with the exception of the green flowlines, which represent rehydrogenation of the surface species.

with Figures 2 and 3 is the presence of the light blue flow lines that represent the radicals provided by the plasma. On the noble catalyst (Ag), we can see that the primary source for ethane production is now C_2H_5* hydrogenation, as opposed to CH_3* coupling in thermal NOCM (see Figure 2) and in NOCM through vibrational excitation of methane (see Figure 3). Also, C_2H_3* and CH_3* are hydrogenated to ethylene and methane, respectively. This indeed shows that, for more noble catalysts, high coverages do not stop the conversion process as hydrogenation reactions occur easily due to the significant densities of the H atoms in the plasma. CH_2* coupling barriers are lower than CH_3* coupling barriers, and thus, for ethylene formation, this pathway has a higher relative weight than the C_2H_3* hydrogenation pathway, in contrast with the analogous reactions for ethane. In general, the blue flow lines corresponding to dehydrogenation processes (see Figures 2 and 3) are now replaced by hydrogenation reactions (green flow lines), both on Ag and on Rh. The only exception is the dehydrogenation of plasma-produced C_2H_3 on Rh, which is the primary source for hydrogen for this type of catalysts. The relative thickness of the product lines shows the selectivity on both catalysts: $C_2H_4 > CH_4 > C_2H_6 > C_2H_2$ on Ag and $C_2H_2 \sim C_2H_4 > C_2H_6 > CH_4$ on Rh.

Future Work. Relative thermal NOCM rates across metals have not been reported as these materials are not common NOCM catalysts, and the reaction is severely equilibrium-limited at the temperatures considered here. The primary aim of this work is to establish the potential for plasma species to promote NOCM across a series of metal catalysts. For this comparison, we assume the plasma species concentrations to be insensitive to the catalyst itself, neglecting, e.g., electrical effects of the catalyst material or the impact of the produced and consumed species on the plasma composition. Such insight cannot as easily be gathered through experimental means because experimental measurements fail to isolate the different aspects of the plasma−catalyst coupling.

The most common experimental techniques available to clarify reaction pathways in plasma catalysis are (i) studying the apparent energy barrier to identify the rate-limiting steps, (ii) isotope experiments to trace back the atomic composition of the products, and (iii) X-ray photoelectron spectroscopy and in situ operando FTIR to study the coverage of the catalyst surface. These techniques can give specific kinetic and mechanistic information, and it would be highly interesting to compare our modeling results and insights with such experimental data, if they become available for NOCM. In addition, our reported model and results allow future work that couples this model to a plasma model, which can calculate actual conversions, yields, and selectivities.[20]

The sections above discuss the plasma−catalyst interactions from a chemical perspective, studying the reactions of plasma species on transition metals. The densities of plasma species are herein assumed unaffected by the presence of the catalyst. For a future more quantitative study on plasma-catalytic NOCM in DBDs, one has to consider the changes in the plasma due to the catalyst material. The introduction of a packing in a DBD can cause an electric field enhancement, depending on the dielectric constant of the material.2846,[47] This results in higher electron temperatures and more effective electron impact reactions (i.e., excitation, dissociation, and ionization of methane). Nozaki *et al.*[48] calculated how the electric field impacts the fragmentation pattern of methane for reduced electric fields (E/N) ranging from 80 to 500 Td. They showed that 60% of the dissociated methane ends in CH_3 radicals and 10% in CH radicals at low E/N, while the fractions at high E/N are 25 and 20%, respectively. The fraction of CH_2 radicals remains unchanged at around 20% for all E/N. The discussions in the sections above demonstrate the importance of the individual densities of each radical species on the selectivity of the C_2 hydrocarbons, and it is to be expected that, for lower electric fields, more ethane is formed due to the higher density of CH_3 radicals, while higher electric fields would benefit the production of acetylene due to higher densities of CH radicals.

For low weight percentages of the metal catalyst on the support, the electrical changes are presumably mostly determined by the support and unaffected by the catalyst material, and the effect of the support could in principle be

https://dx.doi.org/10.1021/acssuschemeng.0c00906
ACS Sustainable Chem. Eng. 2020, 8, 6043−6054

incorporated in the same modeling framework. Higher weight percentages would require studying the effects of the individual metals. As explained in the Introduction, Jo *et al.*[28] studied the effects of an electrically conductive Pt catalyst on the methane reforming inside a DBD. The higher ethane and lower acetylene yields upon introduction of a Pt catalyst compared to bare Al_2O_3 were explained by a lowering of the E/N, causing a higher fraction of CH_3 and a lower fraction of CH radicals.

Additionally, the presence of a packing material in the discharge zone also causes lower electron densities due to neutralization at the bead surface[46] and could change the discharge type from filamentary to surface discharges.[49] It would depend on the plasma and catalyst nature on how these different effects impact the densities of the reactive plasma species.

CONCLUSIONS

Model results show that both vibrational excitations and plasma-generated radicals can impact the rates and selectivity of NOCM on transition metal catalysts. The central concepts of the traditional volcano behavior remain valid when including (plasma-induced) vibrational excitations, but both vertical shifts (higher rates) and horizontal shifts (other catalyst binding strength) can be observed. Plasma-generated radicals affect the turnover frequencies in a different way with mixed selectivity and a limited increase in TOF on more strongly binding catalysts and high selectivity toward ethylene and a much greater increase in TOF on the more noble catalysts. Optimal catalyst materials for thermal catalytic conversion and even for vibrationally excited methane act very differently when put in contact with methane plasmas containing high concentrations of radicals.

The more noble catalysts (e.g., Ag) remain relatively inactive when combined with plasma that is dominated by vibrational excitation, yielding low TOFs and highest selectivity toward ethane. Conversely, when many radicals are present in the plasma, these catalysts benefit maximally from the available radicals and the catalyst efficiently recombines species toward ethylene. Intermediate catalysts (such as Pt, Rh, and Pd) benefit most from vibrationally excited methane, converting the increased amount of CH_3* radicals to ethylene. In the presence of plasma radicals, the production rate of acetylene increases due to the dehydrogenation of C_2 hydrocarbon radicals. The more strongly binding catalysts (like Ru) are less impacted by changes in the gas-phase species. Product formation rates remain low due to poisoning of the surface and low desorption rates and because plasma effects assist nonrate-limiting steps.

Additionally, depending on the desired product, an optimal vibrational temperature can be found for which the TOF is maximal. Lower vibrational temperatures suffer from high dissociation barriers, while higher vibrational temperatures would poison the catalyst and inhibit the further dehydrogenation processes. Because ethane production directly depends on the dissociation rate of methane and does not require further dehydrogenation, it will always benefit from a higher degree of excitation of the reactant. Ethylene production does require another dehydrogenation step, and the optimal vibrational temperature can be found at 1500 K for Pt, Rh, and Pd. For acetylene, this trend is even stronger and excitations do not significantly improve the production rate, regardless of the catalyst. Limiting the vibrational temperature of the plasma to the optimal temperature, depending on the desired product, can reduce the specific energy input and optimize the energy efficiency.

The increased ethylene TOF and selectivity (on noble catalysts for high radical density plasmas and on intermediate catalysts for high vibrational excitation plasmas) is of particular promise for industrial applications, efficiently converting cheap methane to value-added ethylene. In general, it is clear that catalyst and plasma greatly depend on one another and that the choice of catalyst should not only depend on the desired product but also on the type of plasma and its characteristics (i.e., degree of vibrational excitation and reactivity in terms of radical densities). Choosing the appropriate catalyst can increase the production rate (higher TOF), reduce coke formation (increased coverage of volatile species), optimize the energy efficiency (higher TOF for the same degree of vibrational excitation or gas-phase composition), and decide the selectivity of the reaction products.

ASSOCIATED CONTENT

Supporting Information

The Supporting Information is available free of charge at https://pubs.acs.org/doi/10.1021/acssuschemeng.0c00906.

Extra information and figures on the scaling relations, additional heat maps of the effect of bending modes and heat maps, and steady-state coverages and TOFs for the (111) surfaces (PDF)

AUTHOR INFORMATION

Corresponding Author

Yannick Engelmann − *Department of Chemistry, Research Group PLASMANT, PLASMA and NANOLab Centers of Excellence, Universiteit Antwerpen, 2610, Wilrijk, Antwerp, Belgium;* orcid.org/0000-0002-0894-8192; Email: yannick.engelmann@uantwerpen.be

Authors

Prateek Mehta − *Department of Chemical and Biomolecular Engineering, University of Notre Dame, Notre Dame, Indiana 46556, United States*

Erik C. Neyts − *Department of Chemistry, Research Group PLASMANT, PLASMA and NANOLab Centers of Excellence, Universiteit Antwerpen, 2610, Wilrijk, Antwerp, Belgium;* orcid.org/0000-0002-3360-3196

William F. Schneider − *Department of Chemical and Biomolecular Engineering, University of Notre Dame, Notre Dame, Indiana 46556, United States;* orcid.org/0000-0003-0664-2138

Annemie Bogaerts − *Department of Chemistry, Research Group PLASMANT, PLASMA and NANOLab Centers of Excellence, Universiteit Antwerpen, 2610, Wilrijk, Antwerp, Belgium;* orcid.org/0000-0001-9875-6460

Complete contact information is available at: https://pubs.acs.org/10.1021/acssuschemeng.0c00906

Notes

The authors declare no competing financial interest.

ACKNOWLEDGMENTS

We would like to thank Tom Butterworth for his work on methane vibrational distribution functions (VDF) and for sharing his thoughts and experiences on this matter, specifically regarding the VDF of the degenerate modes of methane. We

also acknowledge financial support from the DOC-PRO3 and the TOP-BOF projects of the University of Antwerp. This work was carried out in part using the Turing HPC infrastructure at the CalcUA core facility of the Universiteit Antwerpen, a division of the Flemish Supercomputer Center VSC, funded by the Hercules Foundation, the Flemish Government (Department EWI), and the University of Antwerp. Support for W.F.S. was provided by the National Science Foundation under cooperative agreement no. EEC-1647722, an Engineering Research Center for the Innovative and Strategic Transformation of Alkane Resources (CISTAR). P.M. acknowledges support through the Eilers Graduate Fellowship of the University of Notre Dame.

REFERENCES

(1) Amghizar, I.; Vandewalle, L. A.; Van Geem, K. M.; Marin, G. B. New Trends in Olefin Production. *Engineering* **2017**, *3*, 171−178.
(2) Dry, M. E. High Quality Diesel via the Fischer-Tropsch Process - A Review. *J. Chem. Technol. Biotechnol.* **2002**, *77*, 43−50.
(3) Scapinello, M.; Delikonstantis, E.; Stefanidis, G. D. The Panorama of Plasma-Assisted Non-Oxidative Methane Reforming. *Chem. Eng. Process. Process Intensif.* **2017**, *117*, 120−140.
(4) Horn, R.; Schlögl, R. Methane Activation by Heterogeneous Catalysis. *Catal. Lett.* **2015**, *145*, 23−39.
(5) Vora, B. V.; Marker, T. L.; Barger, P. T.; Nilsen, H. R.; Kvisle, S.; Fuglerud, T. Economic Route for Natural Gas Conversion to Ethylene and Propylene. *Stud. Surf. Sci. Catal.* **1997**, *107*, 87−98.
(6) Torres Galvis, H. M.; De Jong, K. P. Catalysts for Production of Lower Olefins from Synthesis Gas: A Review. *ACS Catal.* **2013**, *3*, 2130−2149.
(7) Guéret, C.; Daroux, M.; Billaud, F. Methane Pyrolysis: Thermodynamics. *Chem. Eng. Sci.* **1997**, *52*, 815−827.
(8) Ma, S.; Guo, X.; Zhao, L.; Scott, S.; Bao, X. Recent Progress in Methane Dehydroaromatization: From Laboratory Curiosities to Promising Technology. *J. Energy Chem.* **2013**, *22*, 1−20.
(9) Xu, Y.; Lin, L. Recent Advances in Methane Dehydro-Aromatization over Transition Metal Ion-Modified Zeolite Catalysts under Non-Oxidative Conditions. *Appl. Catal., A* **1999**, *188*, 53−67.
(10) Mehta, P.; Barboun, P.; Go, D. B.; Hicks, J. C.; Schneider, W. F. Catalysis Enabled by Plasma Activation of Strong Chemical Bonds: A Review. *ACS Energy Lett.* **2019**, *4*, 1115−1133.
(11) Fincke, J. R.; Anderson, R. P.; Hyde, T.; Detering, B. A.; Wright, R.; Bewley, R. L.; Haggard, D. C.; Swank, W. D. Plasma Thermal Conversion of Methane to Acetylene. *Plasma Chem. Plasma Process.* **2002**, *22*, 105−138.
(12) Snoeckx, R.; Bogaerts, A. Plasma Technology-a Novel Solution for CO_2 Conversion? *Chem. Soc. Rev.* **2017**, *46*, 5805−5863.
(13) Neyts, E. C.; Ostrikov, K. (. K.).; Sunkara, M. K.; Bogaerts, A. Plasma Catalysis: Synergistic Effects at the Nanoscale. *Chem. Rev.* **2015**, *115*, 13408−13446.
(14) Yang, Y. Direct Non-Oxidative Methane Conversion by Non-Thermal Plasma: Modeling Study. *Plasma Chem. Plasma Process.* **2003**, *23*, 327−346.
(15) Bogaerts, A.; Neyts, E. C. Plasma Technology: An Emerging Technology for Energy Storage. *ACS Energy Lett.* **2018**, *3*, 1013−1027.
(16) Kogelschatz, U. Dielectric-Barrier Discharges: Their History, Discharge Physics, and Industrial Applications. *Plasma Chem. Plasma Process.* **2003**, *23*, 1−46.
(17) Nozaki, T.; Muto, N.; Kado, S.; Okazaki, K. Dissociation of Vibrationally Excited Methane on Ni Catalyst: Part 1. Application to Methane Steam Reforming. *Catal. Today* **2004**, *89*, 57−65.
(18) Nozaki, T.; Okazaki, K. Non-Thermal Plasma Catalysis of Methane: Principles, Energy Efficiency, and Applications. *Catal. Today* **2013**, *211*, 29−38.
(19) Indarto, A.; Coowanitwong, N.; Choi, J.-W.; Lee, H.; Song, H. K. Kinetic Modeling of Plasma Methane Conversion in a Dielectric Barrier Discharge. *Fuel Process. Technol.* **2008**, *89*, 214−219.
(20) De Bie, C.; Verheyde, B.; Martens, T.; Van Dijk, J.; Paulussen, S.; Bogaerts, A. Fluid Modeling of the Conversion of Methane into Higher Hydrocarbons in an Atmospheric Pressure Dielectric Barrier Discharge. *Plasma Processes Polym.* **2011**, *8*, 1033−1058.
(21) Neyts, E. C.; Bogaerts, A. Understanding Plasma Catalysis through Modelling and Simulation—a Review. *J. Phys. D: Appl. Phys.* **2014**, *47*, 224010.
(22) Puliyalil, H.; Lašič Jurković, D.; Dasireddy, V. D. B. C.; Likozar, B. A Review of Plasma-Assisted Catalytic Conversion of Gaseous Carbon Dioxide and Methane into Value-Added Platform Chemicals and Fuels. *RSC Adv.* **2018**, *8*, 27481−27508.
(23) Chen, H. L.; Lee, H. M.; Chen, S. H.; Chao, Y.; Chang, M. B. Review of Plasma Catalysis on Hydrocarbon Reforming for Hydrogen Production-Interaction, Integration, and Prospects. *Appl. Catal., B* **2008**, *85*, 1−9.
(24) Van Durme, J.; Dewulf, J.; Leys, C.; Van Langenhove, H. Combining Non-Thermal Plasma with Heterogeneous Catalysis in Waste Gas Treatment: A Review. *Appl. Catal., B* **2008**, *78*, 324−333.
(25) Rouwenhorst, K. H. R.; Kim, H.-H.; Lefferts, L. Vibrationally Excited Activation of N_2 in Plasma-Enhanced Catalytic Ammonia Synthesis: A Kinetic Analysis. *ACS Sustainable Chem. Eng.* **2019**, 17515.
(26) Kim, J.; Abbott, M. S.; Go, D. B.; Hicks, J. C. Enhancing C-H Bond Activation of Methane via Temperature-Controlled, Catalyst-Plasma Interactions. *ACS Energy Lett.* **2016**, *1*, 94−99.
(27) Kim, J.; Go, D. B.; Hicks, J. C. Synergistic Effects of Plasma-Catalyst Interactions for CH_4 Activation. *Phys. Chem. Chem. Phys.* **2017**, *19*, 13010−13021.
(28) Jo, S.; Kim, T.; Lee, D. H.; Kang, W. S.; Song, Y.-H. Effect of the Electric Conductivity of a Catalyst on Methane Activation in a Dielectric Barrier Discharge Reactor. *Plasma Chem. Plasma Process.* **2014**, *34*, 175−186.
(29) Schmidt-Szałowski, K.; Krawczyk, K.; Młotek, M. Catalytic Effects of Metals on the Conversion of Methane in Gliding Discharges. *Plasma Processes Polym.* **2007**, *4*, 728−736.
(30) Młotek, M.; Sentek, J.; Krawczyk, K.; Schmidt-Szałowski, K. The Hybrid Plasma-Catalytic Process for Non-Oxidative Methane Coupling to Ethylene and Ethane. *Appl. Catal., A* **2009**, *366*, 232−241.
(31) Spiess, F.-J.; Suib, S. L.; Irie, K.; Hayashi, Y.; Matsumoto, H. Metal Effect and Flow Rate Effect in the Hydrogen Production from Methane. *Catal. Today* **2004**, *89*, 35−45.
(32) Scapinello, M.; Delikonstantis, E.; Stefanidis, G. D. A Study on the Reaction Mechanism of Non-Oxidative Methane Coupling in a Nanosecond Pulsed Discharge Reactor Using Isotope Analysis. *Chem. Eng. J.* **2019**, *360*, 64−74.
(33) Mehta, P.; Barboun, P.; Herrera, F. A.; Kim, J.; Rumbach, P.; Go, D. B.; Hicks, J. C.; Schneider, W. F. Overcoming Ammonia Synthesis Scaling Relations with Plasma-Enabled Catalysis. *Nat. Catal.* **2018**, *1*, 269−275.
(34) Mehta, P.; Barboun, P. M.; Engelmann, Y.; Go, D. B.; Bogaerts, A.; Schneider, W. F.; Hicks, J. C. *Plasma-Catalytic Ammonia Synthesis Beyond the Equilibrium Limit*; ChemRxiv: 2020, DOI: 10.26434/chemrxiv.11768718.v1.
(35) Juurlink, L. B. F.; Killelea, D. R.; Utz, A. L. State-Resolved Probes of Methane Dissociation Dynamics. *Prog. Surf. Sci.* **2009**, *84*, 69−134.
(36) Hummelshøj, J. S.; Abild-Pedersen, F.; Studt, F.; Bligaard, T.; Nørskov, J. K. CatApp: A Web Application for Surface Chemistry and Heterogeneous Catalysis. *Angew. Chem., Int. Ed.* **2012**, *51*, 272−274.
(37) Wang, S.; Petzold, V.; Tripkovic, V.; Kleis, J.; Howalt, J. G.; Skúlason, E.; Fernández, E. M.; Hvolbæk, B.; Jones, G.; Toftelund, A.; Falsig, H.; Björketun, M.; Studt, F.; Abild-Pedersen, F.; Rossmeisl, J.; Nørskov, J. K.; Bligaard, T. Universal Transition State Scaling Relations for (de)Hydrogenation over Transition Metals. *Phys. Chem. Chem. Phys.* **2011**, *13*, 20760−20765.

https://dx.doi.org/10.1021/acssuschemeng.0c00906
ACS Sustainable Chem. Eng. 2020, 8, 6043−6054

(38) Wang, S.; Temel, B.; Shen, J.; Jones, G.; Grabow, L. C.; Studt, F.; Bligaard, T.; Abild-Pedersen, F.; Christensen, C. H.; Nørskov, J. K. Universal Brønsted-Evans-Polanyi Relations for C-C, C-O, C-N, N-O, N-N, and O-O Dissociation Reactions. *Catal. Lett.* **2011**, *141*, 370−373.
(39) Ma, H.; Schneider, W. F. Structure- and Temperature-Dependence of Pt-Catalyzed Ammonia Oxidation Rates and Selectivities. *ACS Catal.* **2019**, *9*, 2407−2414.
(40) Butterworth, T. D.; Amyay, B.; Bekerom, D. v. D.; Steeg, A. v. D.; Minea, T.; Gatti, N.; Ong, Q.; Richard, C.; van Kruijsdijk, C.; Smits, J. T.; van Bavel, A. P.; Boudon, V.; van Rooij, G. J. Quantifying Methane Vibrational and Rotational Temperature with Raman Scattering. *J. Quant. Spectrosc. Radiat. Transfer* **2019**, *236*, 106562.
(41) Fridman, A. *Plasma Chemistry*; Cambridge University Press: 2008, DOI: 10.1017/CBO9780511546075.
(42) Campbell, C. T.; Sprowl, L. H.; Árnadóttir, L. Equilibrium Constants and Rate Constants for Adsorbates: Two-Dimensional (2D) Ideal Gas, 2D Ideal Lattice Gas, and Ideal Hindered Translator Models. *J. Phys. Chem. C* **2016**, *120*, 10283−10297.
(43) Jones, G.; Jakobsen, J. G.; Shim, S. S.; Kleis, J.; Andersson, M. P.; Rossmeisl, J.; Abild-Pedersen, F.; Bligaard, T.; Helveg, S.; Hinnemann, B.; Rostrup-Nielsen, J. R.; Chorkendorff, I.; Sehested, J.; Nørskov, J. K. First Principles Calculations and Experimental Insight into Methane Steam Reforming over Transition Metal Catalysts. *J. Catal.* **2008**, *259*, 147−160.
(44) Lapton, R. *IPython / Jupyter Sankey diagram widget*. https://github.com/ricklupton/ipysankeywidget (accessed Feb 27, 2020).
(45) Berthelot, A.; Bogaerts, A. Modeling of CO_2 Splitting in a Microwave Plasma: How to Improve the Conversion and Energy Efficiency. *J. Phys. Chem. C* **2017**, *121*, 8236−8251.
(46) Van Laer, K.; Bogaerts, A. Influence of Gap Size and Dielectric Constant of the Packing Material on the Plasma Behaviour in a Packed Bed DBD Reactor: A Fluid Modelling Study. *Plasma Processes Polym.* **2017**, *14*, 1−11.
(47) Van Laer, K.; Bogaerts, A. How Bead Size and Dielectric Constant Affect the Plasma Behaviour in a Packed Bed Plasma Reactor: A Modelling Study. *Plasma Sources Sci. Technol.* **2017**, *26*, No. 085007.
(48) Nozaki, T.; Hattori, A.; Okazaki, K. Partial Oxidation of Methane Using a Microscale Non-Equilibrium Plasma Reactor. *Catal. Today* **2004**, *98*, 607−616.
(49) Wang, W.; Kim, H.-H.; Van Laer, K.; Bogaerts, A. Streamer Propagation in a Packed Bed Plasma Reactor for Plasma Catalysis Applications. *Chem. Eng. J.* **2018**, *334*, 2467−2479.

https://dx.doi.org/10.1021/acssuschemeng.0c00906
ACS Sustainable Chem. Eng. 2020, 8, 6043−6054